CARBON ANODE MODELING FOR ELECTRIC ENERGY SAVINGS IN THE ALUMINIUM REDUCTION CELL

D. H. Andersen[1,2], Z. L. Zhang[2]
[1]Hydro Primary Metal Technology, Årdal, Norway
[2]Dept. of Structural Engineering, Norwegian University of Norway

Abstract

The carbon anode geometrical design influences the energy consumption in aluminium production. A 2D finite element model (FE-model) of an anode immersed in an aluminium reduction cell has been developed to study how the anode geometry affects the variation in the anode to cathode distance (ACD). Large variation in ACD will prevent a systematic reduction of the average ACD and thereby hindering a reduction of electrical power loss in the bath. Another modeling example focuses on the large amount of energy loss occurring at the anode-cast iron interface due to the roughness-induced contact resistance. An analytical equation for the real contact area has been established to link the electrical power loss from the contact resistance with the pressure-dependent interface properties. The proposed contact model can be implemented in a full scale electrical FE-analysis of an anode, and used to optimize energy savings.

Introduction

Over the last 10 years there has been focus on current increase actions and also on reducing the noise in the ACD resistance in the aluminium industry. One of the major improvements of reducing the noise was the implementation of slots in the wear surface as illustrated in Figure 1 [1]. The produced carbon dioxide creates bubbles in the bath and the slots function as an escape route for the bubbles. The low frequency noise components in the liquid metal have also been studied in a magneto hydro dynamic (MHD) aspect that has influenced design optimizations of the cell and also the bus bar system. There is also a focus on how the non homogeneous density of the bath creates non homogeneous ACD's [2]. This gives motivation for alumina distribution to the cell through individual feeder control in order to reduce the density differences in the bath. Still there exist variations in the ACD resistance. In normal situations today it is reported that the standard deviation in the current load on individual anodes in the same cell often are more than 10% of the average current [3]. Actions for reducing the noise in the ACD resistance by slots in the anode has also lead to negative effects on other parameters, like current efficiency and increased non homogeneous anode consumption. It is emphasized that slot implementation must be treated individually for each plant in order to avoid pitfalls [4]. The numerical results of the initial state of the anode electrical current was used to analytically describe how this will affect the variation in the anode- to cathode distance (ACD) in a steady state scenario after several hours in the electrolysis bath.

Holms equation of contact resistance [5] is an example of how the contact area between two rough surfaces is used. The contact resistance is present due to asperities ("hills") on the rough surface which makes up the real contact in the interface. An asperity profile function has been proposed that describes the isotropic rough surface of a material. The function is parameterized with three new roughness parameters that control the root mean square height, the slope and the curvature of the rough surface, respectively. Unlike the roughness parameters used in the well known Greenwood-Williamson (GW) model [6,7], the three parameters introduced in this paper are independent of each other, which is an advantage as this facilitates the characterization of the isotropic random surface of the material [8,9,10,11]. However, a disadvantage with this parameterization is that the roughness parameters are not linked to a contact area equation any more, like the Hertz equations that express contact with linear materials. Different asperity profiles defined by the new roughness parameters were analyzed by a 2D axial symmetric FE-model. The numerical results suggest a procedure for developing a contact area function that are parameterized with the three new roughness parameters, which is also suitable for non linear brittle materials. The real contact area function can be used to compute the contact resistance in the carbon-cast iron interface in different ways; either by implementing the equations in new finite contact elements, or in a boundary condition in a FE-model. The paper will first focus on the effect from electric current distribution in the anode and secondly the contact resistance in the cast iron-anode interface.

Parameterization of non homogeneous properties in the cell

We can introduce a parameter, k, describing a relation of ideal electrical current density, J_2, in the inner leg of the anode and a current density, J_3, in the outer leg of the anode as shown in Figure 1. The current density, J_3, can be taken as an abnormal current density and J_2 as a reference current density.

For the ideal initial state, $k=k_0$, (assuming no non homogeneous bath effects change the current distribution) we have

$$J_3 = k_0 J_2 = \frac{I_3}{A_3} = k_0 \frac{I_2}{A_2} \tag{1}$$

where I_2 I_3, A_2, A_3 are currents and cross sections of leg 2 and 3. For the ideal steady state, after several hours in the bath, different processes like surface overvoltage on anode wear surface, production of CO_2 and anode consumption will result in a homogeneously distributed current near the anode wear surface. This means that $k - 1$ and $J_3 = kJ_2 = J_2$, and the initial degree of non homogeneous current distribution, k_0, has been transferred over to the steady state by equation 2.

$$A_3 R_3 = k_0 A_2 R_2$$
$$A_3 \left(R_{an3} + R'_{ba3} \right) = A_2 k_0 \left(R_{an2} + R'_{ba2} \right) \tag{2}$$

The components in the equation are illustrated in Figure 2 which shows the equivalent DC circuits of the anode in the bath. The high resistances in the cell and the resistances that are highly affected by the current density are included in the equivalent DC

circuit (the Nernst potential, anode concentration overvoltage and the cathode overvoltage are therefore neglected).
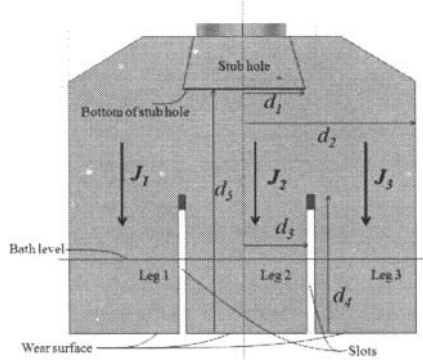

Figure.1. The anode immersed in the electrolysis bath (the longitudinal direction of the anode is into the paper). The slots divide the lower part of the anode into three longitudinal "legs" with height d_4. Dimension d_1 is the radius of the stub hole bottom.

When the resistances in the equation are expressed with its conductivities and dimensions ($R = {}^l/_{\sigma A}$) we get

$$\frac{l_3}{\sigma_{an3}} + \frac{L - l_3}{\sigma'_{ba3}} = k_0 \frac{l_2}{\sigma_{an2}} + k_0 \frac{L - l_2}{\sigma'_{ba2}} \tag{3}$$

We assume homogenous conductivity in the anode and introduce the conductivity relations $m = {}^{\sigma_{an}}/_{\sigma'_{ba2}}$ and $n = {}^{\sigma'_{ba3}}/_{\sigma'_{ba2}}$. Equation 3 can then be expressed as

$$l_3 = \frac{k_0 n l_2 + k_0 mn(L - l_2) - mL}{n - m} \tag{4}$$
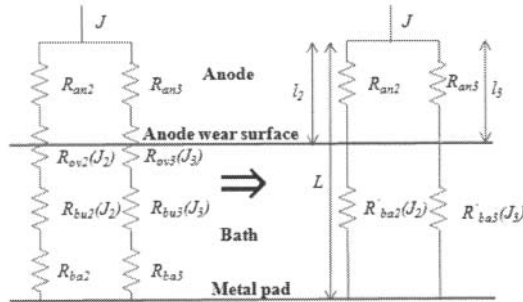

Figure. 2. Equivalent DC circuit of an anode in the bath. The current density, J, is affected by anode resistance, R_{an}, surface overvoltage resistance, R_{ov}, bubble resistance, R_{bu}, and the resistance in the bath, R_{ba}. The left circuit can be simplified to the right DC circuit where R'_{ba} is the resistance that includes R_{ov}, R_{bu} and R_{ba}.

For the case of $n = k_0 = 1$, no difference in the ACD, due to anode design, will appear since $l_3 = l_2$ in equation 4, $ACD_{ref} = L - l_2 = ACD_{abnorm} = L - l_3$, and no non homogeneous anode consumption, due to anode design, will occur. If the reduction cell and the anode are designed and will run with k_0-, m- and n-values that result in $l_3 \neq l_2$ in equation 4, non homogeneous consumption of the anode takes place and a difference in the ACD

appears. Equation 4 can be used in anode design to reduce the ACD when the bath effects on the ACD are isolated (m and n are set to constants). The bath conductivity relation, n, is defined with virtual conductivities. We can express this relation with real physical properties. It is mainly given by phenomena such as surface anode overvoltage and the presence of bubbles in the bath caused by formation of CO_2. From Figure 2, a real physical expression for n can be derived from the voltage drops over each resistance in the bath.

$$\frac{U'_{ba2}}{U'_{ba3}} = \frac{U_{ov2} + U_{bu2} + U_{ba2}}{U_{ov3} + U_{bu3} + U_{ba3}} \tag{5}$$

Equation 5 can further be expressed by resistances and current densities [6] shown in equation 6,

$$\frac{\frac{(L - l_2)J_2}{\sigma'_{ba2}}}{\frac{(L - l_3)J_3}{\sigma'_{ba3}}} = \frac{\frac{RT}{1.08F}\ln\left(\frac{J_2}{J_0}\right) + \frac{d_{b2}J_2}{\sigma_{ba2}(1 - \phi_2)} + \frac{(L - l_2 - d_{b2})J_2}{\sigma_{ba2}}}{\frac{RT}{1.08F}\ln\left(\frac{J_3}{J_0}\right) + \frac{d_{b3}J_3}{\sigma_{ba3}(1 - \phi_3)} + \frac{(L - l_3 - d_{b3})J_3}{\sigma_{ba3}}} \tag{6}$$

where R is the universal gas constant, F the Faraday constant, J_0 the limiting current density in the surface overvoltage term, and d_b the bubble layer thickness which has a tendency to decrease with current in an electrolysis cell [12]. The bubble coverage, Φ, increases with the current density and isolates the anodes wear surface with bubbles in a higher degree [13]. We rearrange equation 6 to find $n = {}^{\sigma'_{ba3}}/_{\sigma'_{ba2}}$. The expression for n can also be modified and include extra effects like anodic- and cathodic concentration overvoltage in the bath. The voltage drops from these effects must be added on the right side of equation 5 and a modified expression for n is derived from the extended equation (an extra resistance in each branch in the left DC circuit in Figure 2 will appear). We can also simplify equation 6 if the surface overvoltage term is linarized. The current densities, J_2 and J_3, in equation 6 will be omitted. The anode-bath conductivity relation, m, has also a virtual component in its expression. This can also be represented with physical parameters by Ohms law. From $U = RI, R = {}^l/_{\sigma A}$ and using Figure 2, the physical expression for m is shown in equation 7.

$$m = \frac{\sigma_{an}}{\sigma'_{ba2}} = \frac{\sigma_{an} A_{an} U_{ba\_meas}}{ACD_{ref} I_{an}} \tag{7}$$

The area, A_{an}, is the anode wear surface, σ_{an} the anode conductivity, $ACD_{ref} = L - l_2$ the reference ACD, I_{an} the electrical current through one anode, and U_{ba_meas} is the measured/calculated voltage drop between the anode and the metal. The real conductivity of the bath is normally around 200 – 300 S/m. The total virtual conductivity of the bath, σ'_{ba} (Figure 2), which also includes surface overvoltage and bubble overvoltage, will be much less. For example, a conservative cell with ACD_{ref}=0.04m and I_{an}=8 000 A is about $m \approx 195$. There is a different m for each aluminium plant and it depends on how the manager decides to run the cell. For a current increase project in a plant the reference ACD will be decreased. Typical values [14] can be ACD_{ref}= 0.03m and a chosen I_{an}= 10 000 A. This results in $m \approx 220$ from equation 7. In the numerical study k_0 will be determined and the results will be linked to the variation in the ACD in equation 4 with specific values on m and n. It is not the

intention of this paper to calculate m and n for many different aluminium reduction cells. The purpose of this paper is to define the parameters and illustrate them with one cell solution ($m = 200$, $ACD_{ref} = 0.04$m).

Results and Discussions of the FE-Analyses on Anode Current Distribution

In the numerical 2D analyses the electric current has been parameterized to enter in four different ways; i_0: upper half of stub hole wall, i_1: whole stub hole wall, i_2: the whole stub hole (wall and bottom) and i_3: bottom of stub hole. The slots got two different depths, $\beta = {}^{d_5}/_{d_4} = \{1.4, 1.75\}$ and positioned at $\gamma = {}^{d_3}/_{d_1} = \{1.00, 1.176, 1.357\}$ (Figure 1). Data for estimating k_0 was found on the boundary 2 cm above the bath shown in Figure 3 (or 17 cm above the anode wear surface). The current density, J_3, is found by integrating the current along the boundary crossing the outer leg of the anode. The current density, J_2, is found by integrating the current along the boundary crossing the inner leg of the anode.

The conductive Media DC module in the FE-software, COMSOL 3.4, was used with 2D quadratic Lagrange elements. A mesh was defined for the whole domain with maximum element size scaling factor = 0.08, element grow rate = 1.2, mesh curvature factor = 0.25, mesh curvature cutoff = 0.0003, resolution of narrow regions = 1. This gave an element number of 75 000 for the whole domain shown in Figure 3.
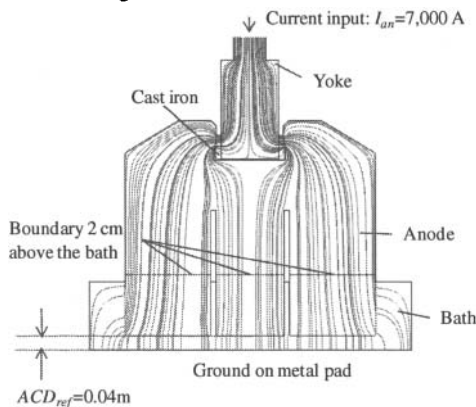

Figure. 3. The 2D domain consists of the sub domains yoke, cast iron, anode and bath. The current enters from the top of the yoke and penetrate down to the metal pad defined as the boundary of ground. All other outer boundaries got an electrical insulated property. Here the current distribution is shown with current setting, i_0.

The best case, $k_0 = 1.06$, has a slot position of $\gamma = 1$, slot depth of $\beta = 1.4$ and electrical current input setting, i_3. This is an anode with deeper slots closer to each other, and with an electrical current entering the anode in the bottom of the anode stub hole. The worst case found from the numerical analyses, $k_0 = 1.20$, has a slot position of $\gamma = 1.36$, slot depth of $\beta = 1.75$ and electrical current input setting, i_0. This is an anode with shorter slots further away from each other, and with electrical current entering in the upper half region of the conic stub hole wall. The current density

distribution along the boundary 2 cm above the bath level for the best- and worst k-case is shown in Figure 4.
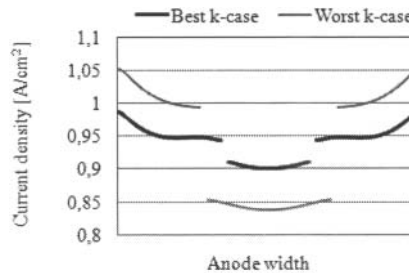

Figure. 4. Electrical normal current density distribution over the anode width along the boundary 2 cm above the bath for the best k-case ($k_0 = 1.06$ for $\gamma = 1, \beta = 1.4, i = i_3$) and worst k-case ($k_0 = 1.20$ for $\gamma = 1.36, \beta = 1.75, i = i_0$). The boundary line is shown in Figure 3.

With k_0 found above, and with a simulated cell setting of $m = 200$ we can set these values into equation 4 and study how an initial current distribution in the anode can affect the ACD. Figure 5 describes the critical n (n_c) we must have for keeping $l_2 = l_3$ for different k_0 when $m = 200$, using equation 4. The worst case of anode design, $k_0 = 1.20$, demands a bath conductivity relation, $n = 0.83$, to avoid a variation in the ACD by k_0. If $n = 0.9$, it is seen from Figure 6 that ${}^{l_2}/_{l_3} = 1.006$. With $l_2 = 600$ mm, we have $l_3 = 596.5$ mm, which means a difference in the ACD of 3.5 mm. Values of k_0, found from realistic anode designs, can easily induce a difference in the ACD around 10% of its value if the critical n is not reached. We should keep in mind that the k_0 found from the numerical analyses are based on average values of current densities. In real cases, if we take into account non homogeneous frozen bath on the anode wear surface, the "real k" can be much higher than the model shows.
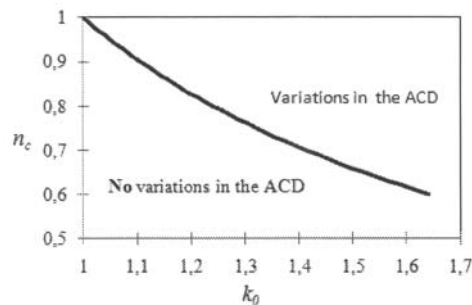

Figure. 5. The critical n for different k_0 to keep $l_2 = l_3$ so that no difference in the ACD will occur. The anode-bath conductivity relation is set to $m = 200$, $ACD_{ref} = 0.04m$ and $l_2 = 600$ mm in equation 4.

It can also increase by asymmetric electrical coupling of the yoke to the anode with cast iron. The electrical coupling between the stub holes in one anode can also differ and increase k_0. A real k_0 of 1.4 demands a bath conductivity relation, $n < 0.71$, if a variation in the ACD is to be avoided (Figure 5). Another point to remember is that the bubble coverage under the anode wear

surface as function of anode current density has a lower slope for current densities above 1 A/cm² than for current densities beneath 1 A/cm² [13].
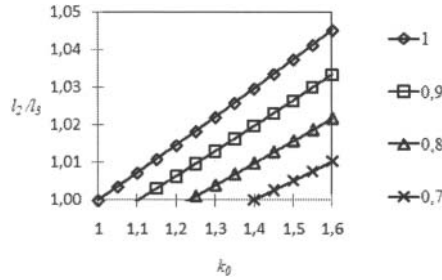

Figure. 6. The relation l_2/l_3 as function of initial anode current distribution, k_0, and the bath conductivity relation, n, for a reference anode height, $l_2 = 600$ mm, $m = 200$ and $ACD_{ref} = 0.04$ m.

This means that the bath conductivity relation, n, is larger for high amperage cells. The risk is higher that the initial electrical current distribution in the anode creates variations in the ACD for a high amperage cell.

Parameterized Contact area function

The contact resistance in the cast iron-yoke interface is present due to rough surfaces, where the "hills" (asperities) on the surface makes contact and decides the real contact area. The real contact area is therefore a sum of contact "islands" within the nominal contact area.
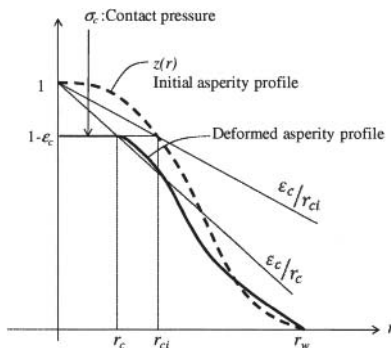

Figure. 7. Schematic drawing of an asperity profile compressed by a contact pressure down to a new height, $z_c = 1 - \varepsilon_c$, and contact radius, r_c . The asperity is axial symmetric about the z-axis. The initial asperity profile is given by the developed function, $z(r)$.

For the cast iron – anode interface, the contact resistance has earlier been found experimentally [15], and laboratory data have been curve fitted [16] to find expressions for the contact resistance, mainly as a function of pressure and temperature. In this paper it has been focused to find an expression of the contact resistance by parameters describing the roughness of the interface, and how the roughness changes by the contact pressure. This can improve the accuracy of calculating the contact resistance for different anode stub hole designs A single asperity (one single contact "island") on the rough isotropic surface was analyzed in a 2D axial symmetric model in COMSOL 3.5. The asperity was

compressed for different initial profiles decided by the developed profile function, $z(r)$. From each of the numerical analyses the contact radius, r_c, contact stress, σ_c, and contact strain, ε_c, was found. The profile function, $z(r)$, was developed and parameterized with three independent roughness parameters. A roughness parameter with similar properties as the known rms roughness is chosen to be the dimensionless crest factor, C_{cr}, (peak- to rms height ratio defined in equation 11). If the peak height is constant, the crest factor has a linear relation to the rms height of the asperity. The crest factor does not need to change if the territorial width of the profile changes. The territorial width can be linear to the rms slope of the profile if the peak height is 1. The second roughness parameter is therefore defined as the width-to peak height ratio, $r_w = r_w/l$, and illustrated in Figure 7. It should be noted that r_w and C_{cr} are dimensionless since they are ratios of distances. These two roughness parameters can also be made independent of each other; they do not need to correlate. The roughness parameter, r_w , has similar properties to the well known density roughness parameter, $D = \#summits/Apparent\ Area$, since they both contain information of the territory of an asperity and the frequency of asperities along the surface. The third roughness parameter is a shape parameter, $\beta^\dagger$, describing a shape of the profile in the same way as the circular shape parameter, β, in the GW-model. When both the rms slope and rms height for a profile is set (and peak height is unity), the profile is still free to vary its curvature within these limits. This means that the shape parameter, $\beta^\dagger$, is defined to take those shapes that do not alter the rms height and the rms slope of the profile. The shape parameter can therefore generate different shapes instead of only one specific shape as the circular shape described by β in the GW-model. The proposed profile function defines it in more detail below. The shape parameter has to change the curvature within a peak height of unity and a constant finite width. This can be fulfilled by moving the function downward along the negative z-axis, but at the same time keep the maximum value of the function equal to 1. The first version of the profile function can now be given in equation 8:

$$z(r) = \frac{1 + \beta^\dagger}{\left(1 + \left(\frac{r}{r_{3dB}}\right)^{2q}\right)^{0.5}} - \beta^\dagger \qquad (8)$$

The shape parameter, $\beta^\dagger$, is defined in the range, $0 < \beta^\dagger < 1$, due to the unity of the peak height (and $0 \le z \le 1$). Now, we want to find an expression for the order, $2q$. It should be expressed by the width of the asperity at $z=0$. We solve for $2q$ by setting $z(r_w=0)$. The order is then given by

$$2q = \frac{\ln\left(\frac{1 + 2\beta^\dagger}{\beta^{\dagger 2}}\right)}{\ln\left(\frac{r_w}{r_{3dB}}\right)} \qquad (9)$$

We set equation 9 into equation 8 and get the asperity profile function in equation 10.

$$z(r) = \cfrac{1+\beta^\dagger}{\left(1+\left(\cfrac{r}{r_{3\,dB}}\right)^{\cfrac{\ln\left(\cfrac{1+2\beta^\dagger}{\beta^{\dagger 2}}\right)}{\ln\left(\cfrac{r_w}{r_{3\,dB}}\right)}}\right)} - \beta^\dagger \qquad (10)$$

Now we have two of the defined roughness parameters in the equation. We still miss the crest factor. Instead of expressing $z(r)$ with r_{3dB}, we rather exchange it with the crest factor. The crest factor, C_{cr}, of $z(r)$ from equation 10 is given as the peak- to rms height ratio in equation 11.

$$C_{cr} = \cfrac{z(0)}{\sqrt{\cfrac{1}{r_w}\int_0^{r_w}|z(r)|^2 dr}} \qquad (11)$$

Equation 11 was solved for different values on $r_w, r_{3dB}, \beta^\dagger$, since the whole symbolic equation is not solvable. It was found that the ratio, r_{3dB}/r_w, has a power relation, $aC_{cr}^{\ b} + c$, for each value of $\beta^\dagger$.

$$r_{3dB} = \left(a(\beta^\dagger)C_{cr}^{b(\beta^\dagger)} + c(\beta^\dagger)\right)r_w \qquad (12)$$

$$r_{3\,dB} = \left(\left(1.034\cdot\beta^{\dagger 3} - 0.7977\cdot\beta^{\dagger 2} + 0.6285\cdot\beta^\dagger + 1.012\right)\cdot\right.$$
$$C_{cr}^{\left(-0.2371\cdot\beta^{\dagger 2} + 1.701\cdot\beta^\dagger - 1.976\right)} + \left(-1.03\cdot\beta^{\dagger 3} + 0.7892\cdot\beta^{\dagger 2}\right.$$
$$\left.\left. - 0.6236\cdot\beta^\dagger - 0.01087\right)\right)\cdot r_w$$

$$0 \le z \le 1, 0.1 \le \beta^\dagger \le 0.9$$
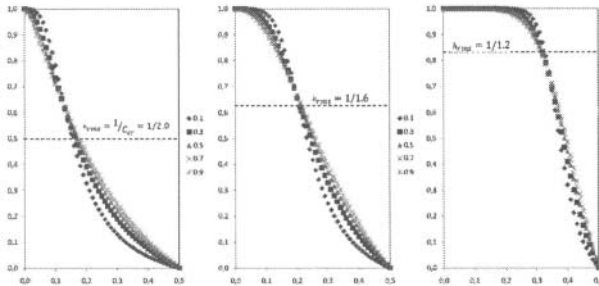$$0 < r_{3dB} < r_w, 1 < C_{cr} \le 2.0, r_w > 0$$

Figure. 8. Plots of the asperity profile function $z(r)$ given in equation 10 and 12 with $r_w=0.5$ for all the plots. Each of the three figures is plotted with five different shapes, $\beta^\dagger$. The five different shapes in each plot have a common crest factor; left plot with $C_{cr}=2.0$, middle plot with $C_{cr}=1.6$ and the right plot with $C_{cr}=1.2$.

The power fit was better than $R^2=0.9998$, where R^2 is the coefficient of determination (on 50 samples within $0 < r_{3dB}/r_w < 1$ for each $\beta^\dagger$ in the range,$0 < \beta^\dagger < 1$). Each coefficient, a, b, c, in the power relation is a function of $\beta^\dagger$ so that r_{3dB} can be expressed as in equation 12. The coefficients of equation 12 were found for nine values on $\beta^\dagger$ from 0.1 stepped with 0.1 up to 0.9. The polynomial fits described in equation 12 of each coefficient was

better than $R^2=0.9995$. If we set r_{3dB} in equation 12 into equation 10, we have the complete asperity profile function with three independent roughness parameters, $r_w, C_{cr}, \beta^\dagger$.

The function, $z(r)$, shown in Figure 8 and expressed in equations 10 and 12, can appear complicated. But r_{3dB} is only a single value when the roughness parameters are set. It contains no argument, r, of the function. The argument of $z(r)$ occurs only once in equation 10, and the order ($2q$) of r is also a single value when the roughness parameters are set. This simplifies mathematical handling considerably.

In the numerical analyses a 2D axial model was used due to the symmetry of the asperity. Special attention has been paid to the mesh of the asperity, with a maximum element length of 1e-4 in the boundary of contact, element growth rate of 1.2 and mesh curvature factor of 0.1. Triangular elements were chosen for the asperity and quadrilateral elements for the smoothed stiff material which compressed the asperity downward. The number of elements varied with the roughness parameters since the area of the material changes. The yield stress, σ_{ys}, of the anode material was set to $20\,MPa$. The stress-strain curve of the material followed the Ramberg-Osgood stress-strain relation. The hardening parameter, n, represents a linear material for $n=1$ and ideal plastic material for $n \to \infty$. The material was analyzed for $n = \{1,2,3,4\}$, with a degree of plasticity far greater than a carbon material, which in many cases are regarded as a linear material.

The general yield offset value was set to $\varepsilon_{pys} = \alpha\,\sigma_{ys}/E = 0.002$. The parameter, α, was set to 1 for all the numerical analyses. All the asperity profiles were analyzed with contact strains, $\varepsilon_c \ge 1\%$. Asperities with low crest factors have been analyzed for contact strains greater than 1%, so that all asperities have reached the limit, $\sigma_c = 3\sigma_{ys}$. One specific asperity was compressed to 3% contact strain. For the territorial radius, two values were chosen; one minimum value of 0.5, and a maximum value of 1.3 ($r_w = \{0.5, 1.3\}$). For the crest factor, five values were tested, $C_{cr} = \{1.2, 1.4, 1.6, 1.8, 2.0\}$. The hardening value was tested with four values of $n = \{1,2,3,4\}$. For the shape parameter, only the value of $\beta^\dagger = 0.1$ was used. The variation in the shape parameter creates only a small variation in the contact area compared to the other roughness parameters, r_w and C_{cr}. We therefore focused on the parameters that created large variations in the contact area. This resulted in a set of 2x5x4x1=40 parametric numerical models, where each model was displacement controlled.

Results and Discussions of the parameterized contact function

From the numerical analyses it was found that the contact radius had to be scaled by the contact strain, as ε_c/r_c which is the same as the mean slope of the compressed "vanished" part of the asperity profile (Figure 7). When this ratio became a function of the ratio, ε_c/r_{ci}, it was observed a high degree of linearity regardless of all the parametric settings in the numerical study, as shown in Figure 9. The proposed form of the function for expressing the contact radius is given in equation 13, where the argument is ε_c/r_{ci}, and the parameters are $C_{cr}, r_w, \beta^\dagger, n$, and $r_{ci}=r(z_c)=r(1-\varepsilon_c)$ from equation 10 and 12 and Figure 7.

$$\frac{\varepsilon_c}{r_c} = a_1\left(\frac{\varepsilon_c}{r_{ci}}\right)^{a_2} = a_1(C_{cr}, r_w, \beta^\dagger, n)\left(\frac{\varepsilon_c}{r_{ci}}\right)^{a_2(C_{cr}, r_w, \beta^\dagger, n)} \qquad (13)$$

1013

Condition: $\left\{ {}^{\sigma_{ys}}\!/_E = const., \varepsilon_{p_{ys}} = const. \right\}$ or $\left\{ \left(\varepsilon_{p_{ys}} \right)_{min} < \right.$ $\left. \varepsilon_{p_{ys}} < \left(\varepsilon_{p_{ys}} \right)_{max} \right\}$

All the curves are above the bold line, $y=x$, in Figure 9. This means that $r_c < r_{ci}$ (except for the zero displacement case where $r_c < r_{ci}$). The four types of effects in Figure 9 are forcing the curves to a lower slope, which means they increase the contact area of an asperity. For an ideal plastic material ($n \rightarrow \infty$) the curves will follow the line, $y=x$, since $r_c \rightarrow r_{ci}$ (the deformation is following the original profile). A decreasing crest factor, $C_{cr} \rightarrow 1$ (solid cylinder) will also force the curves close to $y=x$ (if we neglect the Poisson effect). The linear properties of the function in equation 13 holds also for contact strains larger than 1%. The asperity, $\{r_w = 0.5, C_{cr} = 1.6, \beta^\dagger = 0.1, n = 3\}$, was numerically compressed to 3% contact strain, and the linear property shown in Figure 9 was maintained.
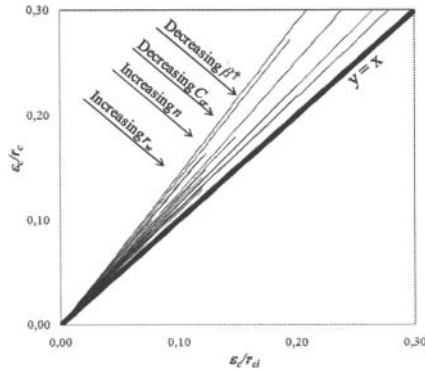

Figure. 9. The function, ${}^{\varepsilon_c}\!/_{r_c}$ versus ${}^{\varepsilon_c}\!/_{r_{ci}}$, for all the numerical results.

There are many reasons for the function, in equation 13, to be solvable by curve fitting: 1) A wide range in each of the roughness parameters in equation 13 give values of ${}^{\varepsilon_c}\!/_{r_c}$ in almost the same range. 2) The high degree of linearity of the function in equation 13 makes it solvable by curve fitting. 3) All the parameters have a property of converging the slope of the function to 1 (${}^{\varepsilon_c}\!/_{r_c} = 1 {}^{\varepsilon_c}\!/_{r_{ci}}$), as shown in Figure 9: i) A lower crest factor, C_{cr}, will move the profile towards a cylindrical shape (Figure 8). Without any Poisson effect, r_c is approximated to r_{ci} for a crest factor equal to 1 (solid cylindrical asperity). ii) A larger r_w will increase the average of r_c for the same variation in the other parameters in equation 13. iii) A smaller $\beta^\dagger$ will transfer more mass of the asperity to the peak (figure 8) and reduce the local slope around the peak, and r_c has to increase. iiii) A higher degree of plasticity (increasing n) will reduce the difference between r_c and r_{ci}.

The contact radius (contact area) of one asperity on the rough surface can therefore be found if the contact strain, ε_c, is known and used in equation 10 with the right values on the defined roughness parameters to find the argument, ${}^{\varepsilon_c}\!/_{r_{ci}}$. The argument, ${}^{\varepsilon_c}\!/_{r_{ci}}$, and the values of the parameters is set into equation 13 which computes the ratio, ${}^{\varepsilon_c}\!/_{r_c}$, to determine the contact radius. The asperities can be distributed along a surface width a

distribution in the roughness parameters. As long as the distributions are known, the total real contact area will be a sum of each distributed asperity.

Conclusions

For realistic anode designs the k_0, describing the degree of initial non homogeneous electrical current distribution in the anode, can range from 1.06 to 1.20 (from 2D modeling). If the anode is designed with a $k_0 = 1.20$, the bath conductivity relation, n, should be less than 0.83 for the analyzed cell if the variation in the ACD is to be avoided. The best k-case (low k_0) describes an anode with deeper slots closer to each other, and with an electrical current entering the anode in the lower parts of the anode stub hole. For an isotropic non linear brittle material the contact area of a rough surface can be found from a function that is parameterized with three new roughness parameters and the hardening value of the material. The independence of the parameters facilitates the characterization of random rough surface and increases the probability to develop contact area functions from regression and curve fitting of data from numerical studies.

References

[1]   M. W. Meier, R. C. Perruchoud, W. K. Fischer. "Production and performance of slotted anodes". Light Metals 2007, 277-282.

[2]   B. Moxnes, A. Solheim, M. Liane, E. Svinsås, A. Halkjelsvik. "Improved cell operation by redistribution of the alumina feeding". Light Metals 2009, 461-466.

[3]   A. Solheim, B. Moxnes. "Anodic Current Distribution in Aluminium Electrolysis Cells". Paper presented at the XIII International conference "Aluminum of Siberia-2007", Krasnoyarsk, Russia, September 11-13, 2007, 21-27.

[4]   X. Wang, G. Tarcy, S. Whelan, S. Porto, C. Ritter, B. Quellet, G. Homley. "Development and Deployment of slotted anode technology at ALCOA". Light Metals 2007, 299-304.

[5]   R. Holm. "Electric Contacts". Springer 1967.

[6]   M. Braunovic, V. V. Konchits, N. K. Myshkin. "Electrical Contacts - Fundamentals, Applications and Technology". CRC Press, 2007

[7]   J. A. Greenwood, J. B. R. Williamson. "Contact of nominally flat surfaces". Proceedings of the Royal Society, A295: pp 300-319, 1966

[8]   D. J. Whitehouse, J. F. Archard. "The properties of random surface of significance of contact". Proc. Roy. Soc. Lond., A316: pp 97-121, 1970

[9]   Myshkin, N. K., "Tribology of electrical contacts", In Tribology in the USA and Former Soviet Union, Allerton Press, New York, pp. 341-364, 1994

[10]   B. Bhushan. "Contact Mechanics of rough surfaces in tribology: multiple asperity contact", Tribology Letters, 4: pp 1-35, 1998

[11]   R. A. Onions, J. F. Archard. "The contact of surfaces having a random structure". J. Phys. D, Appl. Phys., 6: pp 289-304, 1973

[12]   W. Haupin. "Interpreting the components of the cell voltage". Light Metals 1998, 531-537.

[13]   N. Richards, H. Gulbrandsen, S. Rolseth, J. Thonstad. "Characterization of the fluctuation in anode current density and "bubble events" in industrial reduction cells". Ligth Metals 2003, 315.322.

[14]   A. Solheim. "Anode-Cathode Distance in ÅI and ÅII". Internal Report 2008, Sintef Materials and Chemistry.

[15]   M. Sørlie, H. Gran, Cathode collector bar-to-carbon contact resistance, Light Metals, 1992, 779-787

[16]   D. Richard, M. Fafard, R. Lacroix, P. Clery, Y. Maltais. "Thermo-Electro-Mechanical Modeling of the Contact between Steel and Carbon Cylinders using the Finite Element Method", Light Metals 2000, 523-528.